

Article

Designing Strain-Less Electrode Materials: Computational Analysis of Volume Variations in Li-Ion and Na-Ion Batteries

Maxime Maréchal ^{1,2}, Romain Berthelot ^{1,2}, Patrick Rozier ^{2,3}  and Matthieu Saubanère ^{1,2,4,*} ¹ ICGM, Université de Montpellier, CNRS, ENSCM, Montpellier, France² Réseau sur le Stockage Electrochimique de l'Energie (RS2E), 80039 Amiens, France³ CIRIMAT Université Toulouse 3 Paul Sabatier, Toulouse INP, CNRS 118 Route de Narbonne, 31062 Toulouse cedex 9, France⁴ Université de Bordeaux, CNRS, LOMA, UMR 5798, F-33400 Talence, France

* Correspondence: matthieu.saubanere@cnrs.fr

Abstract: Mechanical degradation in electrode materials during successive electrochemical cycling is critical for battery lifetime and aging properties. A common strategy to mitigate electrode mechanical degradation is to suppress the volume variation induced by Li/Na intercalation/deintercalation, thereby designing strain-less electrodes. In this study, we investigate the electrochemically-induced volume variation in layered and spinel compounds used in Li-ion and Na-ion battery electrode materials through density functional theory computations. Specifically, we propose to decompose the volume variation into electronic, ionic, and structural contributions. Based on this analysis, we suggest methods to separately influence each contribution through strategies such as chemical substitution, doping, and polymorphism. Altogether, we conclude that volume variations can be controlled by designing either mechanically hard or compact electrode materials.

Keywords: Li-ion batteries; Na-ion batteries; strain-less electrode; electrode materials; aging properties; mechanical degradation; design principles



Citation: Maréchal, M.; Berthelot, R.; Rozier, P.; Saubanère, M. Designing Strain-Less Electrode Materials: Computational Analysis of Volume Variations in Li-Ion and Na-Ion Batteries. *Batteries* **2024**, *10*, 262. <https://doi.org/10.3390/batteries10080262>

Academic Editor: Seiji Kumagai

Received: 7 June 2024

Revised: 19 July 2024

Accepted: 22 July 2024

Published: 25 July 2024



Copyright: © 2024 by the authors. Licensee MDPI, Basel, Switzerland. This article is an open access article distributed under the terms and conditions of the Creative Commons Attribution (CC BY) license (<https://creativecommons.org/licenses/by/4.0/>).

1. Introduction

Continued advancements in lithium-ion batteries have positioned them as the predominant technology for electrical energy storage. However, current commercial positive electrode materials undergo significant volume changes during cycling, posing challenges to their long-term performance and stability. For instance, positive electrode materials like layered oxides based on Nickel, Manganese, and Cobalt (NMC's) and the spinel LiMn_2O_4 experience notable volume alterations, in particular, when charged to high voltages [1–5]. The mismatch between the lithiated and delithiated structures, differing in volume and shape, induces an important source of strain leading to mechanical stresses, which are at the origin of electrode material degradation and battery performance deterioration after repeated cycles [6–11]. More precisely, these changes affect the general morphology of electrode materials, a well-known cause of capacity loss [7]. The primary particles of the cathode, forming secondary particles, undergo repeated attachment and detachment during charging and discharging due to these volume changes [9,12]. This stress creates cracks inside the particles, leading to a loss of connectivity within the active material. As a consequence, the liquid electrolyte penetrates through these cracks, increasing the cathode electrolyte interface layer. Ultimately, these crystals break down, resulting in significant capacity loss and deterioration of battery performance [13,14]. These electrochemically-induced strains also pose threats to the separator and overall battery safety. In solid-state batteries, issues related to volume changes in positive electrode materials are even more problematic [15–20]. Apart from the formation of cracks and fractures in positive electrode materials, “breathing” electrodes lead to the diminution of the interface between the solid electrolyte and the electrode material, posing risks to the system's integrity. Consequently,

the volume changes in the cathode significantly impact battery performances, affecting long-term stability and discharge capacity, presenting a significant challenge to improving high-energy-density batteries. Hence, the ideal scenario involves employing cathode materials that undergo minimal volume changes and electrochemically-induced strain during lithium intercalation/deintercalation.

Over the leading factor that controls the electrochemically-induced strain, the nature of the Transition Metal (TM) is shown to play a critical role. More precisely, volume variations and capacity fading have been related, and are drastically modified when changing the Co, Mn and Ni ratios in NMC materials. In particular, high Ni content leads to significant volume changes and mechanical degradation at high voltage [13,21–29]. The crystal structure type is also expected to have a significant impact. For instance, in contrast to layered materials, it has been shown that disordered rocksalts, due to cation mixing which leads to a cubic structure, demonstrate minimal and isotropic volume changes during lithiation and delithiation processes [30–33]. Besides tuning the TM and the structure, various strategies have been proposed to achieve suppressed volume expansion and contraction towards zero-strain positive electrodes. In particular, electrode surface engineering or concentration gradient [27,34–36] and electrode material doping [28,37–41] have become popular.

In order to accelerate the design of strainless electrodes a quantitative or even qualitative evaluation of the different contributions to the electrochemically-induced strain is needed. To that aim, Zhao et al. have linked qualitatively the volumic variation with the t_{2g} versus e_g character of the redox orbital and confirm that isotropic structures are more prone to reduce the volumic variations [33]. In this work, we investigate various factors controlling volume changes upon lithium removal in a family of A_xMO_2 compounds, where A represents an alkali metal (Li or Na) and M represents a 3d TM. Two structural frameworks have been considered, namely the 2D layered and the 3D spinel structures. Firstly, our density functional theory computation shows that high spin (HS) and low spin (LS) TM configurations in the intercalated material drastically affect its cell volume in agreement with the corresponding tabulated ionic radius values. Additionally, van der Walls interactions play a significant role in decreasing the inter-layer spacing and thus the volume of deintercalated layered compounds. In a second step, we propose to decompose the volume variation in terms of ionic, electronic, and structural contributions. Considering the ionic contribution, we show that for Li-based compounds the deinsertion process is fairly compensated by the reminiscent electrostatic repulsion of the surrounding anions in the deintercalated phase. The substitution of Li by Na in a layered electrode leads to an increase of about $\sim 3.5\text{ \AA}^3$ of the cell volume variation per exchanged alkali, which corresponds to the sphere volume difference computed using Li^+ and Na^+ tabulated ionic radii. The electronic contribution is shown to be governed by the nature of the TM and can be estimated using also tabulated ionic radii of both the TM's oxidized and reduced forms. The structural contribution is shown to be important and related to the elasticity of the material. For isotropic compounds, the structural contribution of the volume variation follows the electronic contribution and can be correlated to the isotropic elastic Bulk modulus B_0 . For layered materials the structural contribution follows the ionic contribution and is isotropic, i.e., the cell is stretched/contracted along the c parameter in order to minimize elastic energy since the elasticity perpendicular to the TM layer is lower than the elasticity in the plane parallel to the TM layer. Finally, based on our analysis we propose at the end of the manuscript hints to reduce volume variations by designing harder or more compact electrode materials.

2. Computational Details

We have studied layered A_xMO_2 compounds, where A represents an alkali metal, Li or Na at stoichiometry $x = 0$ or 1 and M represents a 3d TM, ranging from Ti to Ni within the $R-3m$ layered crystal structure. Spinel compounds $\text{Li}_x\text{M}_2\text{O}_4$ within the $Fd-3m$ symmetry group have also been studied for comparison, using the same 3d TM's and for $x = 0$ and 1 . Density functional theory calculations were performed using the Vienna Ab initio

Simulation Package (VASP) [42–44]. It uses a plane wave basis set and pseudopotentials using the projector augmented wave (PAW) potentials [45]. Both the kinetic energy cut-off and k-point grid were tested, with the criterion for convergence being an energy variation of less than 1 meV/atom. A plane wave energy cutoff of minimum 520 eV and a well converged Γ -centered Monkhorst-Pack k-point grid were used in these calculations [46]. The energy difference convergence criteria of the global break condition for the electronic self-consistent loop was set to 10^{-8} eV, whereas the energy difference convergence criteria of the break condition for the ionic relaxation loop was set to 10^{-3} eV. Structural relaxations and energy calculations were performed using the Strongly Constrained and Appropriately Normed (SCAN) functional [47–50] with the inclusion of van der Waals (vdW) interactions by the means of the revised Vydrov–van Voorhis nonlocal correlation functional (rVV10) [51] called hereafter SCAN-rVV10 functional. These relaxations were also performed with the (rotationally invariant) DFT + U approach [52] on top of the Perdew–Burke–Ernzerhof (PBE) functional [53]. On-site Coulomb interaction strength (U) has been specified for each TM following the literature, i.e., $U_{\text{Ti}} = 3.3$ eV, $U_{\text{V}} = 2.5$ eV, $U_{\text{Cr}} = 3.9$ eV, $U_{\text{Mn}} = 3.9$ eV, $U_{\text{Fe}} = 4.2$ eV, $U_{\text{Co}} = 3.2$ eV, $U_{\text{Ni}} = 6.0$ eV. Finally, PBE+U calculations have been performed with and without the inclusion of van der Waals interactions by means of the DFT-D3 method of Grimme et al. [54]. All of these materials were assumed to be ferromagnetic and both the HS and LS configurations were calculated. To access these configurations the difference between the total number of up and down spin electrons was fixed. The atomic charge distribution was computed using the Voronoi deformation density [55].

3. Results

3.1. Volumes and Relation with Ionic Radii

We initially focus on the volume of intercalated compounds shown in Figure 1 and deintercalated compounds in Figure 2, for the considered materials, using different functionals in order to evaluate our theoretical setup. As shown in Figure 1, the relaxed volumes of LiMO_2 and NaMO_2 per formula unit exhibit non-monotonous behavior as a function of the TM for all considered functionals. Considering different functionals, the SCAN-rVV10 compared to the PBE + U + D3 functional leads to a volume compression, while comparing the PBE + U and the PBE + U + D3 functionals leads to a volume dilatation, respectively. When compared with experimental data (see Supplementary Information SI1), a fair agreement is obtained for all functionals, with the PBE + U + D3 functional yielding the best mean errors and deviations. The behavior of the cell volume as a function of the TM is influenced by both the nature of the TM and its spin state. Indeed, as shown in Figure 1c the cell volume is linearly correlated to the ionic volume $V_{\text{Tab}}(\text{M}^{3+}) = 4\pi R_{\text{Tab}}^3(\text{M}^{3+})/3$ in an octahedral environment, where $R_{\text{Tab}}(\text{M}^{n+})$ is the tabulated ionic radius of the metal M in an oxidation state $n+$, regardless of the functional considered. See Supplementary Information SI2 for the considered values of ionic radii. Importantly, the LS versus HS configurations lead to drastically different results for M = Mn, Fe, Co, and Ni (see Supplementary Information SI3a). Concerning the relative stability of the HS vs LS configurations, our calculations indicate that for AMnO_2 the HS configuration is energetically favored, while ACoO_2 and ANiO_2 adopt the LS configuration. LS states are associated with smaller ionic radii compared to HS configurations since for the latter more anti-bonding e_g states are filled and are associated with larger TM-O bonds due to the presence of anti-bonding σ type TM-O bonds. AFeO_2 is predicted to be in the HS configuration with PBE + U and with PBE + U + D3, a result supported by experimental data showing that AFeO_2 compounds are HS in different polymorphs [56]. The SCAN-rVV10 functional also predicts NaFeO_2 to be HS but LiFeO_2 to be LS. Given that the energy difference between the LS and HS configurations is rather low (~ 10 meV/Formula unit), we have considered for LiFeO_2 the results of the HS configuration in the manuscript for the sake of coherence. We observe an important local octahedral Jahn–Teller (JT) distortion which originates from electronic degeneracy in the e_g shell of the AMnO_2 HS (d^4) and ANiO_2 LS (d^7) configurations. As expected, it lowers the $R\text{-}3m$ symmetry to $C2/m$ in the

relaxed structure. A less important JT distortion is observed in AVO_2 and ATiO_2 which originates from the t_{2g} degeneracy. Note, that the JT effect is not supposed to have a huge effect on the cell volume which is supported by the linear relation between the cell volume and the ionic radius. A similar linear relation between the cell volume and ionic volume is obtained considering the spinel structure, using the mean values between the corresponding ionic radius of M in the 3+ and 4+ oxidation states, see Supplementary Information SI4.

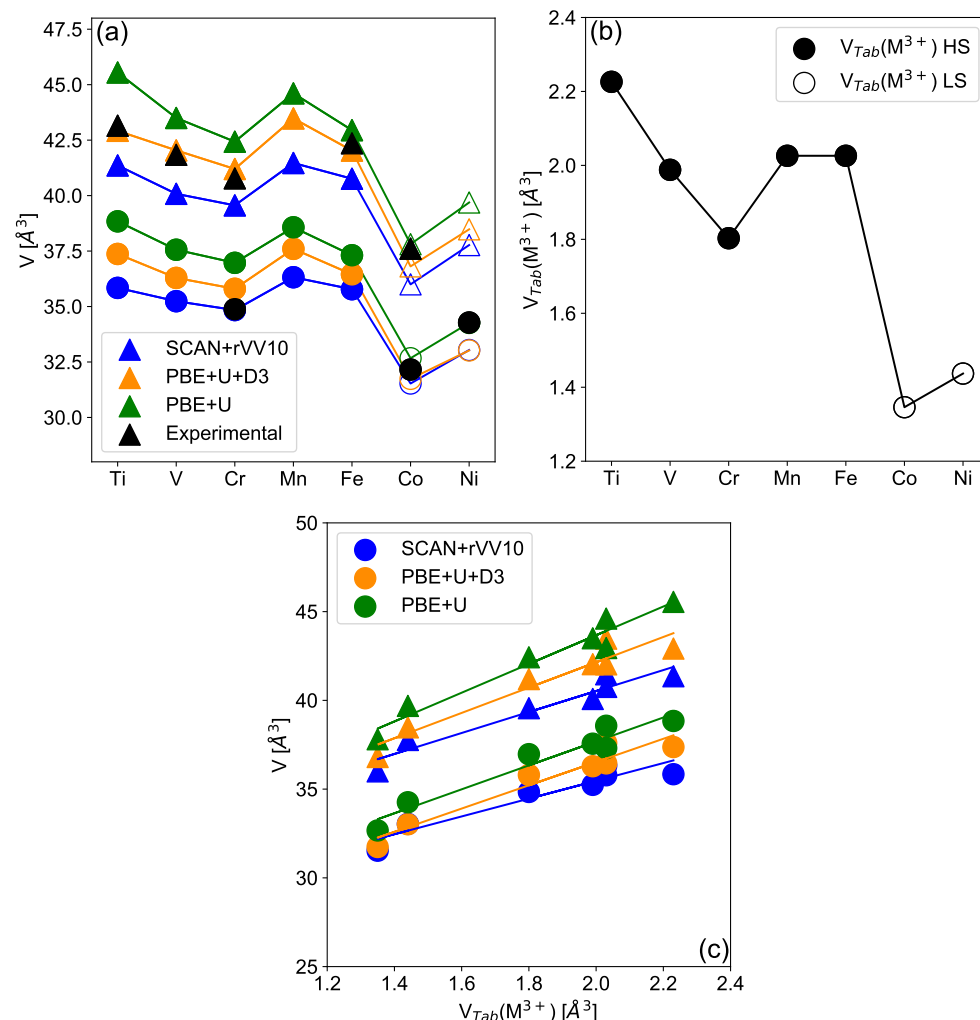


Figure 1. Relaxed volume per MO_2 stoichiometry of layered LiMO_2 and NaMO_2 **(a)** materials for different 3d transition metals ranging from Ti to Ni. Results are given for the lowest energy spin configuration obtained using different functionals, namely PBE + U (green symbols), PBE + U + D3 (orange symbols) and SCAN-rVV10 (blue symbols) compared with experimental data obtained from the literature (black symbols). Filled and open symbols correspond to the HS and LS states respectively. Tabulated ionic volume **(b)** for the LS and HS configurations of the different 3d transition metals in their +III state and in an octahedral environment. In **(c)** is shown the correlation between the relaxed volume of LiMO_2 (circles) and NaMO_2 (triangles) with the ionic volume computed using tabulated ionic radii (see text for details). Lines are guides for the eyes.

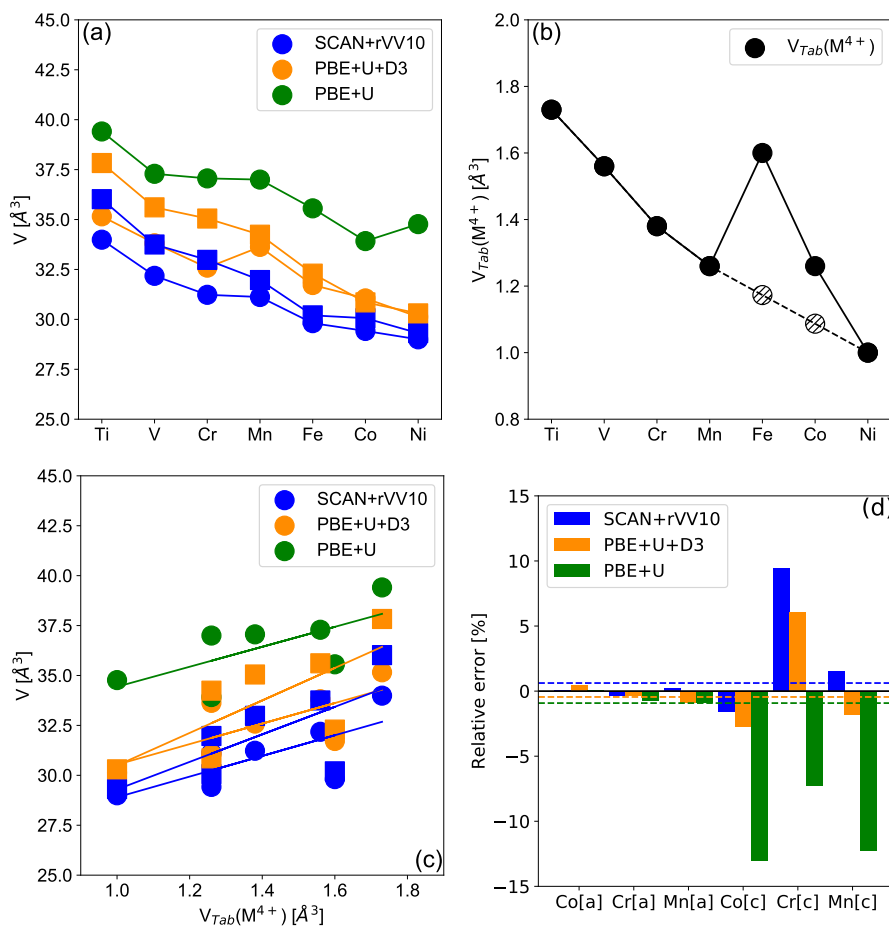


Figure 2. (a) Relaxed volume per MO_2 unit of deintercalated MO_2 for the layered (circle) and spinel (square) polymorphs for different 3d transition metals ranging from Ti to Ni. Results are given for the lower energy spin configuration obtained using different functionals, namely PBE + U (green symbol), PBE + U + D3 (orange symbols) and SCAN-rVV10 (blue symbols) also compared with experimental volumes obtained from the literature. Color and symbol codes are consistent in all subfigures. (b) Tabulated ionic values of the TM's in their +IV state in an octahedral environment. Hatched values for Fe and Co are calculated from the interpolation between Mn and Ni. (c) The correlation between the relaxed volume of MO_2 and the ionic volume was computed using tabulated ionic radii. In (a–c) lines are guides for the eyes, and results are given for the LS/HS configuration leading to the minimum energy. (d) Relative difference (in %) between relaxed and experimental cell parameters [57–60] a and c for layered materials. The dashed lines represent the mean relative error for each functional.

In Figure 2, volumes of deintercalated MO_2 layered and spinel compounds are shown, with M ranging from Ti to Ni, and as a function of the tabulated ionic volume of M^{4+} for different functionals. In contrast with intercalated compounds, no ambiguities regarding the spin state emerge from our calculations, FeO_2 , CoO_2 , and NiO_2 being in the LS configuration. Concerning layered compounds, the volume decays quasi-linearly with the electronic filling which is consistent with a consecutive filling of the t_{2g} orbitals from zero to six electrons. Moreover, Figure 2b shows that similarly for sodiated and lithiated compounds, the volume of the MO_2 structure follows the trend of M^{4+} ionic volumes obtained through tabulated ionic radii, with an exception for the Iron and to a lesser extent for Cobalt compounds. However, the ionic radii provided in the table for Fe^{4+} and Co^{4+} must be approached with caution since the 4+ oxidation state for Fe and Co are quite exotic, as only a few compounds have been isolated; most of them are short-lived intermediaries in reactions, in particular, for Fe. The computed Voronoi volumes in MO_2

compounds show as expected a quasi-linear decay as a function of the electronic filling, see Supplementary Information SI5. A similar trend for the cell volume as a function of the transition metals' ionic radius is observed for spinel compounds. Note, that 3D spinel structures are shown to be more compact than the 2D layered structures. Concerning the functionals' accuracies, the trend of the volume as a function of the considered transition metal appears to be independent of the considered functional. However, the PBE + U functional predicts a volume that is about ~10% above the result obtained using the PBE + U + D3 and SCAN-rVV10 functionals. This overestimation obtained with the PBE+U functional can be attributed to an overestimation of the cell parameter c . Indeed, Figure 2c shows the relative error between experimental and computed a and c lattice parameters for synthesized compounds. While one observes a relatively weak mismatch between experimental and computed values for the a parameter, regardless of the functional, the c parameter is shown to be largely overestimated by the PBE + U functional compared to experimental values. The PBE + U + D3 and SCAN-rVV10 functionals are shown to provide much more reliable results, particularly for layered CoO_2 and NiO_2 . Yet, the large overestimation of the c parameter can be attributed to a poor estimation of the van der Waals interactions, which are better taken into account within the PBE + U + D3 and SCAN + rVV10 functionals. These results highlight the importance of the van der Waals interactions on the structural properties of layered oxides, particularly at low alkali content. For spinel materials, the PBE + U + D3 functional is shown to be sensitively more accurate than the SCAN-rVV10 functional. Altogether, in terms of functional reliability, PBE + U + D3 and SCAN-rVV10 are shown to provide structural parameters consistent with each other and consistent with experimental data when available. A typical margin of error for these functionals on the cell parameters would be around 3 %, so the error on the volume should be of a similar magnitude. On the contrary, the PBE + U functional fails to take into account van der Walls interactions, which leads to a poor description of inter-layer spacing in layered compounds. For this reason, the PBE + U functional is discarded for the rest of the study. In terms of energy, the PBE + U + D3 appears to be more relevant to predict the right LS vs HS configurations but also the electrochemical potentials, see Supplementary Information SI6.

3.2. Electrochemically-Induced Volume Variation

Given the relaxed intercalated and deintercalated volumes, we can define the electrochemically-induced volume variation per alkali $A = \text{Li}$ or Na , following Zhao et al. [33].

$$\frac{\partial V}{\partial n_A} = \frac{V_{A\text{Host}} - V_{\text{Host}}}{n_A} \quad (1)$$

where $V_{A\text{Host}}$ and V_{Host} are the volumes per formula unit (\AA^3) of the intercalated and deintercalated structures, n_A is the number of exchanged alkali per formula unit, and finally $\partial V / \partial n_A$ is a volume per exchanged alkali (\AA^3). In Figure 3 we show $\partial V / \partial n_A$ for the layered Li_xMO_2 , Na_xMO_2 and the spinel $\text{Li}_x\text{Mn}_2\text{O}_4$ materials using the PBE + U + D3 and the SCAN functionals. Interestingly, the profile of $\partial V / \partial n_A$ as a function of the considered TM differs in spinel and layered structures, while it follows the same trend when switching from Li to Na. For layered structures $\partial V / \partial n_{\text{Li}}$ increases quasi-linearly with the electron filling from 2\AA^3 for $M = \text{Ti}$ to 6\AA^3 for $M = \text{Fe}$. Then it is drastically reduced to 2\AA^3 for $M = \text{Co}$ before slightly increasing to 2.5\AA^3 for $M = \text{Ni}$. The evolution is similar for both functionals and for the sodiated compounds but $\partial V / \partial n_{\text{Na}}$ is shifted to higher values following the different ionic radii of Li and Na. For spinel compounds, $\partial V / \partial n_{\text{Li}}$ shows an overall reduced amplitude compared with layered materials, in particular, for $M = \text{Ti}$, V , Cr , Fe and Co . The $\partial V / \partial n_A$ trend appears different between spinel and layered materials suggesting that the crystallographic structure plays an important role in governing $\partial V / \partial n_A$. More precisely, while the cell volume of intercalated and deintercalated phases are shown to be qualitatively related to the ionic volume of the TM, $\partial V / \partial n_A$ does not follow $\Delta V_{\text{Tab}} = V_{\text{Tab}}(\text{M}^{3+}) - V_{\text{Tab}}(\text{M}^{4+})$ for layered electrode materials. Consequently, $\partial V / \partial n_A$

is controlled by the choice of the TM in spinel compounds, (remember that the value of ΔV_{Tab} for iron is questionable) but also note that it is strongly influenced by other factors in layered electrodes. In a previous study, Zhao et al. proposed a qualitative argument to rationalize the amplitude of $\partial V / \partial n_A$ which is governed by the t_{2g} versus e_g character of electronic states implied in the redox process [33]. Indeed, the redox associated with e_g states is expected to lead to larger volume variations than for t_{2g} states since the e_g (t_{2g}) states imply σ (π) type of TM-O bounds, and thus larger (smaller) TM-O distance variation along the redox reaction, respectively. To give rationality to this hypothesis, in Table 1 (d) we show the electronic filling of the e_g / t_{2g} orbitals for the redox active TM's. Following the t_{2g} / e_g rule would imply that the largest value of $\partial V / \partial n_A$ is obtained for Mn (HS), Fe(HS) and Ni (LS) based compounds. For spinel structures, the t_{2g} / e_g rule appears relevant. However, our results suggest that the relation between $\partial V / \partial n_A$ and the redox orbital t_{2g} / e_g character is not straightforward in layered compounds. For instance, $\partial V / \partial n_A$ for the e_g active layered ANiO_2 is lower (or equivalent) than for the t_{2g} active AMO_2 , where M = Ti, Cr and V using the PBE + U + D3 functional. Moreover, the volume variation associated with the deintercalation of an alkali in the HS AFeO_2 compounds is associated with a filling change of two e_g electrons, which is not reflected by the volume variation. Finally, $\partial V / \partial n_{\text{Li}}$ for the HS LiCoO_2 and HS LiNiO_2 compounds, imply a single or double change in the e_g orbital filling, and shows a comparable amplitude for LiCrO_2 , which is associated with a t_{2g} redox.

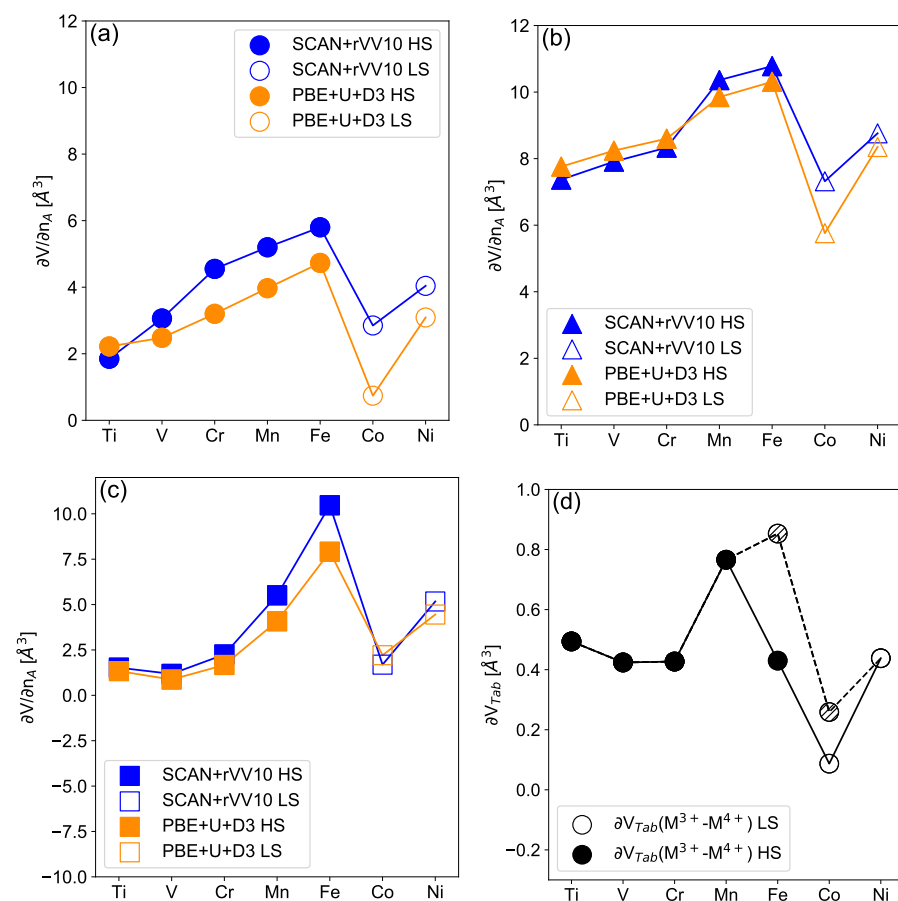


Figure 3. Electrochemically-induced volume variation $\partial V / \partial n_A$ in the lithiated (a), sodiated (b) layered structures and for lithiated spinel (c) structure as a function of the transition metal ranging from Ti to Ni. Results are given for the PBE + U + D3 (orange symbols) and SCAN-rVV10 functionals (blue symbols). Tabulated ionic volume difference (d) between the +IV and +III (HS/LS) states. For all subfigures, filled (open) symbols highlight cases for which the intercalated compound is the most stable within the HS (LS) configuration, respectively. Lines are guides for the eyes.

In order to understand the trend of the electrochemically-induced volume variation per alkali, we aim to decompose it into different contributions. One possible contribution is the term $\partial V^{\text{Ionic}} / \partial n_A$, which represents the effect of removing an alkali ion from the structure. This term is proportional to the ionic volume of the ion in its specific environment, whether it is in an octahedral (Oh) or tetrahedral (Td) coordination. This contribution is expected to weakly depend on the nature of the TM and on the long-range feature of the crystal structure beyond the first coordination sphere. In parallel, we consider an electronic contribution $\partial V^{\text{Elec}} / \partial n_A$ driven by the removal (addition) of electrons in the redox anti-bonding TM-O orbitals. This contribution takes into account the contraction (dilatation) of TM-O bonds upon deintercalation (intercalation), respectively, and is expected to solely depend on the TM's nature and spin configuration. This contribution should be affected by the t_{2g}/e_g nature of the redox center. The decomposition between the different contributions of the electrochemically-induced volume variation can be summarized in the following equation

$$\frac{\partial V}{\partial n_A} = \frac{\partial V^{\text{Ionic}}}{\partial n_A} + \frac{\partial V^{\text{Elec}}}{\partial n_A} + \frac{\partial V^{\text{Host}}}{\partial n_A} \quad (2)$$

where the last term $\partial V^{\text{Host}} / \partial n_A$ corresponds to a contribution that depends on the Host crystal structure and might modulate ionic and electronic contributions.

Table 1. Schematic representation of the electronic configurations of each TM with an oxidation degree of 3+ and 4+, also considering the high spin (HS) or low spin (LS) configurations. Cells in green highlight the lowest energy configuration for unambiguous cases (equivalent lowest energy configurations whatever the considered structure (layered *vs* spinel), alkali (Li *vs.* Na) or functional (PBE + U + D3 *vs.* SCAN-rVV10). Orange cells represent the case of Fe-based compounds which is more controversial and is considered in the HS configuration for layered and spinel compounds (see text for details).

LiMeO ₂ (+III)	Ti (d ¹)	V (d ²)	Cr (d ³)	Mn (d ⁴)	Fe (d ⁵)	Co (d ⁶)	Ni (d ⁷)
HS (T2g/Eg)	↑—	↑↑—	↑↑↑	↑↑↑↑	↑↑↑↑↑	↑↑↑↑	↑↑↑↑
BS (T2g/Eg)				↓↓—↑	↓↓—↑	↓↓—↑	↓↓—↑
MeO ₂ (+IV)	Ti (d ⁰)	V (d ¹)	Cr (d ²)	Mn (d ³)	Fe (d ⁴)	Co (d ⁵)	Ni (d ⁶)
HS (T2g/Eg)	—	↑—	↑↑	↑↑↑	↑↑—	↑↑↑	↑↑↑
BS (T2g/Eg)					↑↑—↑	↑↑—↑	↑↑—↑

The amplitude of the $\partial V^{\text{Ionic}} / \partial n_A$ contribution associated with the addition/removal of an alkali ion is expected to be proportional to the alkali ionic radius. This assumption is confirmed by our calculations, as shown in Figure 4a. Indeed, it shows that $\Delta V_{\text{Na} \rightarrow \text{Li}} = \partial V / \partial n_{\text{Na}} - \partial V / \partial n_{\text{Li}}$ is quasi-constant, i.e., independent of the TM. More precisely, assuming the electronic and structural contributions to be equivalent in iso-structural sodiated and lithiated compounds leads to $\Delta V_{\text{Na} \rightarrow \text{Li}} \sim \partial V^{\text{Ionic}} / \partial n_{\text{Na}} - \partial V^{\text{Ionic}} / \partial n_{\text{Li}}$. Note, that the value of $\Delta V_{\text{Na} \rightarrow \text{Li}} \simeq 5.75 \text{ \AA}^3$ is larger than the difference in atomic volume obtained using tabulated ionic radii $\Delta V_{\text{Tab}} = 4\pi [R_{\text{Tab}}^3(\text{Na}^+) - R_{\text{Tab}}^3(\text{Li}^+)] / 3 = 3.5 \text{ \AA}^3$, which appears coherent since small cations compress all other bonds in the structure, an effect that is known as chemical pressure. To go further into detail, we compute $\partial V^{\text{Ionic}} / \partial n_A$ using the relaxed structure as

$$\frac{\partial V^{\text{Ionic}}}{\partial n_A} = \langle V(\text{LiO}_6) \rangle_{\text{AHost}} - \langle V(\square\text{O}_6) \rangle_{\text{Host}} \quad (3)$$

where $\langle V(\text{AO}_6) \rangle_{\text{AHost}}$ and $\langle V(\square\text{O}_6) \rangle_{\text{Host}}$ represent the mean volume of the AO_6 octahedra computed in the intercalated (AHost) compound and the A-vacancy $\square\text{O}_6$ octahedra measured in the deintercalated (Host) structure. The volumes of the octahedra were calculated using the O-O distances in the relaxed structure. Since the octahedra are not regular, we decomposed them into four tetrahedrons and used the Cayley–Menger determinant to calculate their volumes [61]. Results are presented in Figure 4b for lithiated, sodiated layered materials and lithiated spinel materials. $\partial V^{\text{Ionic}} / \partial n_A$ is shown to be quasi-constant for the spinel structure. It follows a trend similar to $\partial V / \partial n_A$ with an amplitude of ~ 1 (2) \AA^3 between the minima for ACoO_2 and maxima for AFeO_2 for lithiated (sodiated) materials, respectively. Interestingly, a mean difference between trend lines for sodiated and lithiated compounds, $\Delta V_{\text{Na} \rightarrow \text{Li}}^{\text{Ionic}} = \partial V^{\text{Ionic}} / \partial n_{\text{Na}} - \partial V^{\text{Ionic}} / \partial n_{\text{Li}} \simeq 3.5 \text{\AA}^3$ is observed in Figure 4b. This value approximately corresponds to the difference between the volumes of Na and Li calculated using the tabulated ionic radii. The difference between $\Delta V_{\text{Na} \rightarrow \text{Li}}$ and $\Delta V_{\text{Na} \rightarrow \text{Li}}^{\text{Ionic}}$ allows us to evaluate the effect of chemical pressure to be of about $\Delta V_{\text{Na} \rightarrow \text{Li}} - \Delta V_{\text{Na} \rightarrow \text{Li}}^{\text{Ionic}} \sim 2.25 \text{\AA}^3$ by substituting Na for Li. Another important piece of information from Figure 4b concerns the amplitude of $\partial V^{\text{Ionic}} / \partial n_A$. In particular, for lithiated compounds, $\partial V^{\text{Ionic}} / \partial n_{\text{Li}}$ shows an amplitude close to zero reflecting the fact that the volume of removed Li^+ ions is compensated in the delithiated structure by the electrostatic repulsion between oxygen in the vacancy octahedra. Similar results are obtained using the SCAN-rVV10 functional, see Supplementary Information SI7.

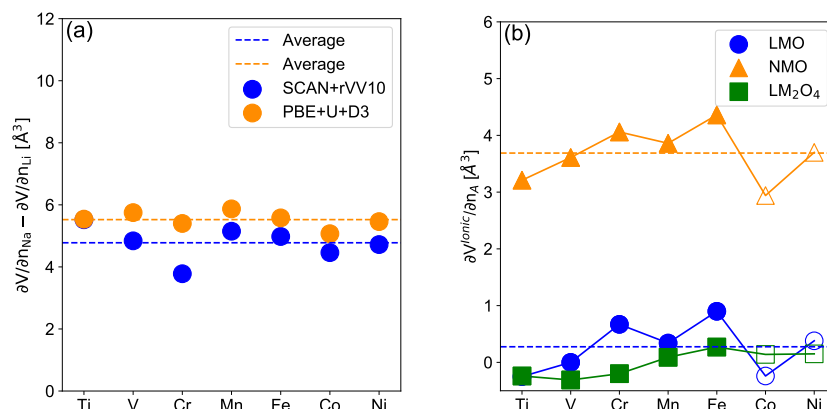


Figure 4. Difference of electrochemically-induced volume variation (a) between the sodiated and lithiated layered materials as a function of the TM for the SCAN-rVV10 (blue circles) and PBE + U + D3 (orange circles) functionals. Ionic contribution (b) of the electrochemically-induced volume variation $\partial V^{\text{Ionic}} / \partial n_A$ as defined in Equation (4) as a function of the TM for layered lithiated (blue circles), sodiated (orange triangles) and lithiated spinel (green squares) materials using the PBE + U + D3 functional. Filled and open symbols correspond to the HS and LS states respectively.

We focus now on the induced volume variation associated with the addition/removal of electrons. In order to evaluate $\partial V^{\text{Elec}} / \partial n_A$ quantitatively, we define the following equation

$$\frac{\partial V^{\text{Elec}}}{\partial n_A} = \langle V(\text{MO}_6) \rangle_{\text{AHost}} - \langle V(\text{MO}_6) \rangle_{\text{Host}} \quad (4)$$

where $\langle V(\text{MO}_6) \rangle_{\text{AHost}}$ ($\langle V(\text{MO}_6) \rangle_{\text{Host}}$) represents the mean volume of the AO_6 octahedra computed in the intercalated (deintercalated) structure, respectively. In Figure 5a we show $\partial V^{\text{Elec}} / \partial n_A$ as a function of the transition metal M for the layered and spinel materials obtained with the PBE + U + D3 functional. Results for $\partial V^{\text{Elec}} / \partial n_A$ appear to be quasi-independent of the considered alkali and the structure type. More precisely, chemical pressure induced by switching from Na to Li does not affect drastically the TM-O bond lengths suggesting that the MO_6 octahedra are the most rigid entities in the structure. This is also supported by the relatively weak influence of the structure on $\partial V^{\text{Elec}} / \partial n_A$. As

expected, $\partial V^{\text{Elec}} / \partial n_A$ is influenced by the t_{2g}/e_g character of the redox orbital showing higher amplitudes for Mn, Fe and Ni-based materials when Mn and Fe are in the HS configuration. $\partial V^{\text{Elec}} / \partial n_A$ represents the specific effects of different transition metals. More precisely, $\partial V^{\text{Elec}} / \partial n_A$ follows the same trend as the variation of the ionic volume computed with the tabulated ionic radii for the transition metal M, $\Delta V_{\text{Tab}}(M)$. Importantly, ΔV_{Tab} is tabulated with respect to the crystal field environment and spin configuration, thus taking into account the change in the t_{2g}/e_g character of the redox orbital. Attention has to be paid to spinel systems. Indeed, some compounds show M^{3+}/M^{4+} disproportionation or charge density wave (CDW) in the intercalated phases while in other materials all of the TM's are equivalent, which probably influences the results shown in Figure 5a. More precisely, as illustrated in Supplementary Information SI8, the PBE + U + D3 functional predicts a CDW for all compounds while SCAN-rVV10 predicts CDW only for M = Mn, Co and Ni-based LiM_2O_4 spinel materials. Note, that the value of $\partial V^{\text{Elec}} / \partial n_A$ is not affected by the occurrence of CDW as the volume of $M^{4+}\text{O}_6$ octahedra in the intercalated structure remains constant upon deintercalation.

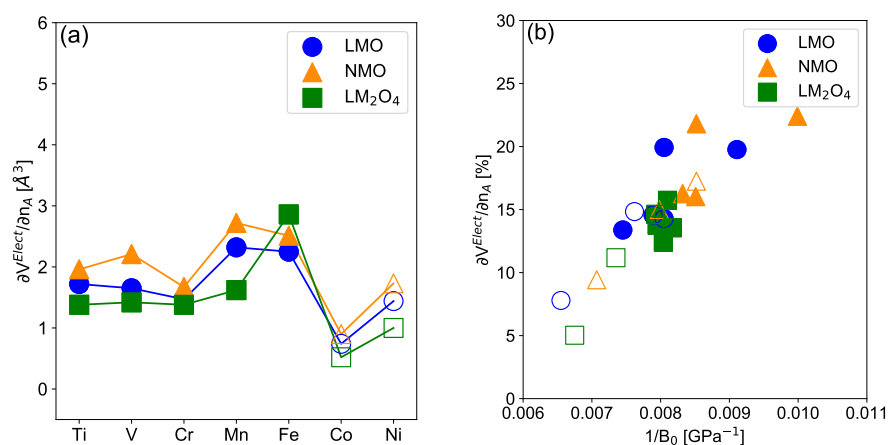


Figure 5. Electronic contribution (a) of the electrochemically-induced volume variation as defined in Equation (4) as a function of the TM for layered lithiated (blue circle), sodiated (orange triangle) and lithiated spinel (green square) materials using the PBE + U + D3 functional. Lines are guides for the eyes. (b) Relation between the electronic part of the total electrochemically-induced strain as a function of the inverse of the Bulk modulus. In all subfigures, filled (Open) symbols correspond to cases where the intercalated compound is in the HS (LS) configuration, respectively.

The $\partial V / \partial n_A$ of the isotropic spinel material appears to be controlled by its electronic part. This is consistent with the fact that the TMO_6 octahedra, being the most rigid part of the structure, should be the limiting factor for the elasticity of the material. Indeed, following Hooke's law, one would expect that the volume change in the host matrix induced by the intercalation is proportional to the elastic modulus of the host matrix which is the case for spinel materials. More precisely, larger (smaller) volume variations $\partial V / \partial n_A$ are associated with lower (higher) bulk modulus, or equivalently, with softer (harder) compounds, respectively. On the contrary, for layered materials, the inverse of the Bulk modulus appears to be linearly correlated to $\partial V^{\text{Elec}} / \partial n_A$ rather than $\partial V / \partial n_A$ as we show in Figure 5. This is consistent with the fact that the bulk modulus or the mechanical hardness of the material is limited by the ionicity of the TM-O bonds, which is governed by the chemical nature of the TM and the electronic filling. Finally, in an anisotropic structure such as layered materials, the volume variation is also anisotropic and consequently it does not appear as directly related to isotropic elastic moduli such as the bulk modulus.

Finally, we show in Figure 6 $\partial V^{\text{Host}} / \partial n_A$ the contribution to the electrochemically induced volume variation. $\partial V^{\text{Host}} / \partial n_A$ follows $\partial V^{\text{Ionic}} / \partial n_A$ for anisotropic layered electrodes but $\partial V^{\text{Elec}} / \partial n_A$ for the isotropic spinels. We found a quasi-perfect linear relation between $\partial V^{\text{Host}} / \partial n_A$ and $\partial V / \partial n_A$ suggesting that $\partial V^{\text{Host}} / \partial n_A$ results from a compromise

between the elasticity along the different TM-O and A-O or \square -O bonds. Moreover, layered material $\partial V^{\text{Host}} / \partial n_A$ (and consequently $\partial V / \partial n_A$) is linearly related to the inverse of the elastic coefficient C_{33} measuring the materials' elasticity in the direction perpendicular to the metallic sheets, see Figure 6c. As evidenced in other layered materials, this direction is supposed to be soft, in particular, in deintercalated material as vacancy-O bonds are expected to be soft [62]. Note, however, that the Jahn–Teller distortion might also influence the elastic coefficient in different directions, in particular, for based Fe and Mn materials, which might explain the non-perfect linear trend observed in Figure 6c. It contrasts with isotropic electrode materials such as spinels for which the elastic coefficient remains equivalent in all the directions such that $\partial V / \partial n_A$ is correlated with the isotropic bulk moduli, as already discussed, dictated by the limiting TM-O bond hardness. Overall, it suggests that the volume variations are dictated by the elasticity of the material and are consequently strongly influenced by the crystal's structure. Yet, the anisotropy of the structure might induce softer (more elastic) directions along which the volume variations are expected to be increased such as for layered materials.

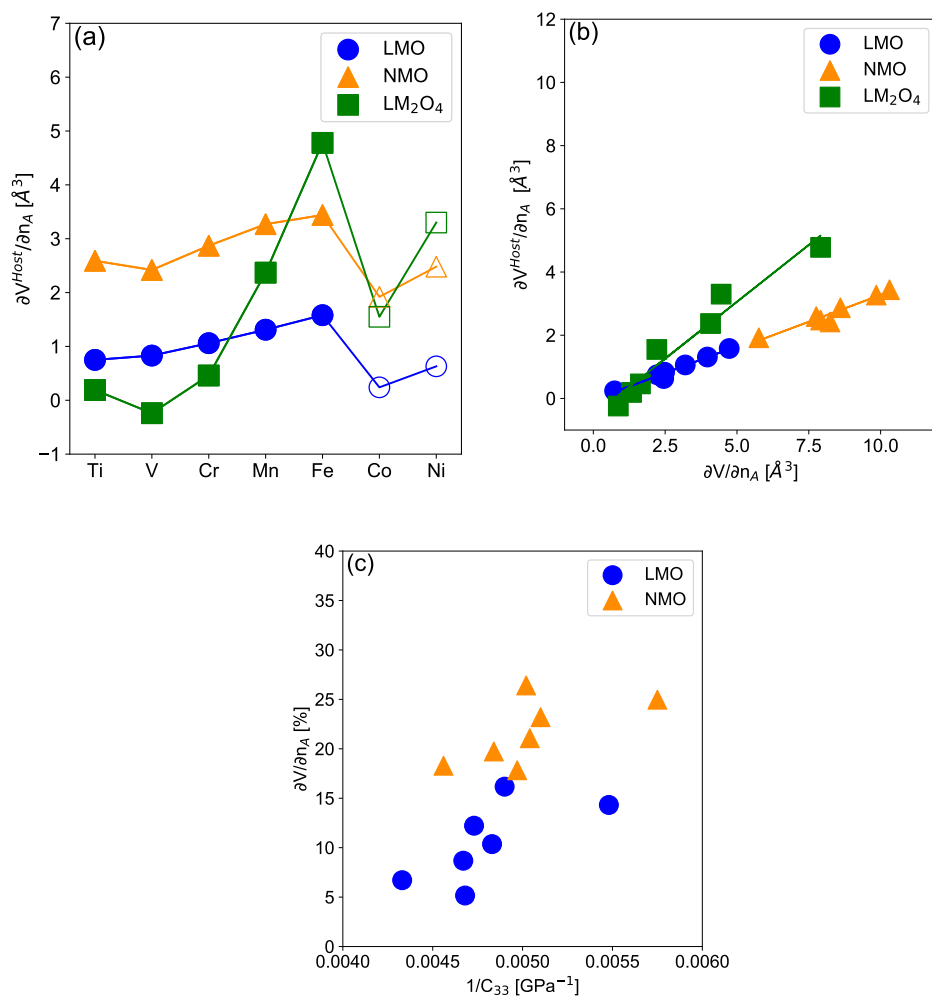


Figure 6. Structural (Host) contribution (a) to the electrochemically-induced volume variation as defined in Equation (4) as a function of the TM for layered lithiated (blue circle), sodiated (orange triangle) and lithiated spinel (green square) materials using the PBE + U + D3 functional. Filled and open symbols correspond to the HS and LS states respectively. (b) Structural (Host) contribution to the electrochemically-induced volume variation as a function of the total electrochemically-induced volume variation. (c) Electrochemically-induced volume variation as a function of the inverse of the elastic constant C_{33} . In all subfigures, filled (Open) symbols correspond to cases where the intercalated compound is in the HS (LS) configuration, respectively. Lines are guides for the eyes.

4. Discussion and Conclusions

By decomposing the electrochemically-induced volume variation ($\partial V / \partial n_A$) between ionic, electronic and structural contributions we have shown that the ionic part depends mainly on the exchanged alkali type, Li vs Na. Moreover, in the case of lithium, the volume loss associated with Li removal is nearly compensated by electrostatic interactions, resulting in an almost negligible effect.

The electronic contribution takes into account the t_{2g}/e_g character of the redox orbital which plays an important role but does not constitute sufficient criteria to be predictive. However, the electronic contribution is shown to govern $\partial V / \partial n_A$ in isotropic materials such as spinels. Fortunately, it can be quantitatively estimated by using tabulated ionic radii associated with the concerned TM in the relevant environment and oxidation state. This appears to be a reliable descriptor to estimate this contribution except for Fe for which the Fe^{4+} tabulated ionic radius has to be questioned.

Finally, the volume variation associated with the Host reaction to the addition of electrons and alkali ions is shown to result from a compromise between the elasticity associated with the different components. De facto, it depends strongly on the anisotropic character of the crystal structure.

Altogether, our results show that the overall volume variations are controlled by the elasticity of the material suggesting that the intercalation is an elastic, thus reversible process. For isotropic structures, the electrochemically induced strain is linearly correlated with the inverse of the Bulk modulus. The case of anisotropic materials is more complex as the elasticity is also anisotropic and the volume variations are consequently expected to be increased in the easiest (softer) direction. Consequently, $\partial V / \partial n_A$ cannot be directly predicted from tabulated ionic volumes or using the isotropic elastic moduli. In the case of layered material, we show that the volume variations are related to the elastic coefficient in the direction perpendicular to the layer that is believed to be lower than in a direction parallel to the layer.

In terms of material design, our results suggest that the most efficient way to reduce electrochemically-induced volume variations, besides manipulating the chemical nature of the alkali or transition metal, is to take advantage of the elastic character of intercalation. As evidence, harder materials, i.e., with higher elastic modulus, will experience fewer volume variations, but they might also be restrained in terms of capacity as the intercalation process might also be limited. The material's hardness can be modulated using, for instance, chemical substitutions. Note, however, that to be efficient, the tuning of the hardness has to be performed isotropically such that no softer direction emerges and cancels the desired effect. Another strategy involves designing compact electrodes, as the volume variation is expected to be proportional to the material's volume in an elastic system. This can be achieved in several ways: by focusing on compact polymorphs (generally 3D rather than 2D), by controlling the spin configurations to be LS, or by chemically doping with "small" ions, such as Al^{3+} . In particular, the doping strategy can be especially efficient if, in addition to reducing the volume, it forces the LS configuration and increases the mechanical hardness of the material.

Supplementary Materials: The following supporting information can be downloaded at: <https://www.mdpi.com/article/10.3390/batteries10080262/s1>; SI0: Crystallographic structures; SI1: Benchmark of cell parameters of $LiMO_2$ AND $NaMO_2$; SI2: Tabulated ionic radii; SI3: Influence of the spin configuration on the cell volume of $LiMO_2$ and $NaMO_2$; SI4: Relation between cell volume and ionic radii in the spinel LiM_2O_4 compounds; SI5: Voronoi volumes and charges for the $LiMO_2$ and MO_2 compounds; SI6: Electrochemical potentials; SI7: Decomposition of the volume variation into ionic, electronic and structural contributions; SI8: M^{3+}/M^{4+} disproportion (cdw) in LiM_2O_4 compounds.

Author Contributions: Conceptualization, M.S.; Methodology, P.R. and M.S.; Formal analysis, M.M., R.B., P.R. and M.S.; Investigation, M.M.; Writing—original draft, M.M. and M.S.; Writing—review & editing, M.M., R.B., P.R. and M.S.; Visualization, M.M.; Supervision, R.B., P.R. and M.S.; Project

administration, M.S.; Funding acquisition, P.R. and M.S. All authors have read and agreed to the published version of the manuscript.

Funding: The authors thank the French National Research Agency (STORE-EX Labex Project ANR-10-LABX-76-01) for financial support.

Data Availability Statement: The original contributions presented in the study are included in the article, further inquiries can be directed to the corresponding authors.

Conflicts of Interest: The authors declare no conflict of interest.

References

- Berg, H. Neutron Diffraction Study of Electrochemically Delithiated LiMn_2O_4 Spinel. *Solid State Ionics* **1999**, *126*, 227–234. [[CrossRef](#)]
- Çapraz, Ö.Ö.; Bassett, K.L.; Gewirth, A.A.; Sottos, N.R. Electrochemical Stiffness Changes in Lithium Manganese Oxide Electrodes. *Adv. Energy Mater.* **2016**, *7*, 1601778. [[CrossRef](#)]
- Kondrakov, A.O.; Schmidt, A.; Xu, J.; Geßwein, H.; Möning, R.; Hartmann, P.; Sommer, H.; Brezesinski, T.; Janek, J. Anisotropic Lattice Strain and Mechanical Degradation of High- and Low-Nickel NCM Cathode Materials for Li-Ion Batteries. *J. Phys. Chem. C* **2017**, *121*, 3286–3294. [[CrossRef](#)]
- Jangid, M.K.; Mukhopadhyay, A. Real-Time Monitoring of Stress Development during Electrochemical Cycling of Electrode Materials for Li-ion Batteries: Overview and Perspectives. *J. Mater. Chem. A* **2019**, *7*, 23679–23726. [[CrossRef](#)]
- Ruess, R.; Schweißler, S.; Hemmelmann, H.; Conforto, G.; Bielefeld, A.; Weber, D.A.; Sann, J.; Elm, M.T.; Janek, J. Influence of NCM Particle Cracking on Kinetics of Lithium-Ion Batteries with Liquid or Solid Electrolyte. *J. Electrochem. Soc.* **2020**, *167*, 100532. [[CrossRef](#)]
- De Biasi, L.; Schwarz, B.; Brezesinski, T.; Hartmann, P.; Janek, J.; Ehrenberg, H. Chemical, Structural, and Electronic Aspects of Formation and Degradation Behavior on Different Length Scales of Ni-Rich NCM and Li-Rich HE-NCM Cathode Materials in Li-Ion Batteries. *Adv. Mater.* **2019**, *31*, 1900985. [[CrossRef](#)] [[PubMed](#)]
- Edge, J.S.; O’Kane, S.; Prosser, R.; Kirkaldy, N.D.; Patel, A.N.; Hales, A.; Ghosh, A.; Ai, W.; Chen, J.; Yang, J.; et al. Lithium Ion Battery Degradation: What You Need to Know. *Phys. Chem. Chem. Phys.* **2021**, *23*, 8200–8221. [[CrossRef](#)]
- Stallard, J.C.; Vema, S.; Hall, D.S.; Dennis, A.R.; Penrod, M.E.; Grey, C.P.; Deshpande, V.S.; Fleck, N.A. Effect of Lithiation upon the Shear Strength of NMC811 Single Crystals. *J. Electrochem. Soc.* **2022**, *169*, 040511. [[CrossRef](#)]
- Stallard, J.C.; Wheatcroft, L.; Booth, S.G.; Boston, R.; Corr, S.A.; De Volder, M.F.; Inkson, B.J.; Fleck, N.A. Mechanical Properties of Cathode Materials for Lithium-Ion Batteries. *Joule* **2022**, *6*, 984–1007. [[CrossRef](#)]
- De Vasconcelos, L.S.; Xu, R.; Xu, Z.; Zhang, J.; Sharma, N.; Shah, S.R.; Han, J.; He, X.; Wu, X.; Sun, H.; et al. Chemomechanics of Rechargeable Batteries: Status, Theories, and Perspectives. *Chem. Rev.* **2022**, *122*, 13043–13107. [[CrossRef](#)]
- Park, S.H.; Lee, N.K.; Lee, S.G.; Han, J.H.; Lee, Y.J. Zero-Strain Cathodes for Lithium-Based Rechargeable Batteries: A Comprehensive Review. *ACS Appl. Energy Mater.* **2023**, *6*, 12–30. [[CrossRef](#)]
- Xu, Z.; Rahman, M.M.; Mu, L.; Liu, Y.; Lin, F. Chemomechanical Behaviors of Layered Cathode Materials in Alkali Metal Ion Batteries. *J. Mater. Chem. A* **2018**, *6*, 21859–21884. [[CrossRef](#)]
- Ryu, H.H.; Park, K.J.; Yoon, C.S.; Sun, Y.K. Capacity Fading of Ni-Rich $\text{Li}[\text{Ni}_x \text{Co}_y \text{Mn}_{1-x-y}] \text{O}_2$ ($0.6 \leq x \leq 0.95$) Cathodes for High-Energy-Density Lithium-Ion Batteries: Bulk or Surface Degradation? *Chem. Mater.* **2018**, *30*, 1155–1163. [[CrossRef](#)]
- Ryu, H.H.; Namkoong, B.; Kim, J.H.; Belharouak, I.; Yoon, C.S.; Sun, Y.K. Capacity Fading Mechanisms in Ni-Rich Single-Crystal NCM Cathodes. *ACS Energy Lett.* **2021**, *6*, 2726–2734. [[CrossRef](#)]
- Koerver, R.; Aygün, I.; Leichtweiß, T.; Dietrich, C.; Zhang, W.; Binder, J.O.; Hartmann, P.; Zeier, W.G.; Janek, J. Capacity Fade in Solid-State Batteries: Interphase Formation and Chemomechanical Processes in Nickel-Rich Layered Oxide Cathodes and Lithium Thiophosphate Solid Electrolytes. *Chem. Mater.* **2017**, *29*, 5574–5582. [[CrossRef](#)]
- Koerver, R.; Zhang, W.; De Biasi, L.; Schweißler, S.; Kondrakov, A.O.; Kolling, S.; Brezesinski, T.; Hartmann, P.; Zeier, W.G.; Janek, J. Chemo-Mechanical Expansion of Lithium Electrode Materials—On the Route to Mechanically Optimized All-Solid-State Batteries. *Energy Environ. Sci.* **2018**, *11*, 2142–2158. [[CrossRef](#)]
- Shi, T.; Zhang, Y.Q.; Tu, Q.; Wang, Y.; Scott, M.C.; Ceder, G. Characterization of Mechanical Degradation in an All-Solid-State Battery Cathode. *J. Mater. Chem. A* **2020**, *8*, 17399–17404. [[CrossRef](#)]
- Doerr, C.; Capone, I.; Narayanan, S.; Liu, J.; Grovenor, C.R.M.; Pasta, M.; Grant, P.S. High Energy Density Single-Crystal NMC/ $\text{Li}_6\text{PS}_5\text{Cl}$ Cathodes for All-Solid-State Lithium-Metal Batteries. *ACS Appl. Mater. Interfaces* **2021**, *13*, 37809–37815. [[CrossRef](#)] [[PubMed](#)]
- Yoon, K.; Kim, H.; Han, S.; Chan, T.S.; Ko, K.H.; Jo, S.; Park, J.; Kim, S.; Lee, S.; Noh, J.; et al. Detrimental Effect of High-Temperature Storage on Sulfide-Based All-Solid-State Batteries. *Appl. Phys. Rev.* **2022**, *9*, 031403. [[CrossRef](#)]
- Kalnaus, S.; Dudney, N.J.; Westover, A.S.; Herbert, E.; Hackney, S. Solid-State Batteries: The Critical Role of Mechanics. *Science* **2023**, *381*, eabg5998. [[CrossRef](#)]

21. Noh, H.J.; Youn, S.; Yoon, C.S.; Sun, Y.K. Comparison of the Structural and Electrochemical Properties of Layered $\text{Li}[\text{Ni}_x\text{Co}_y\text{Mn}_z]\text{O}_2$ ($x = 1/3, 0.5, 0.6, 0.7, 0.8$ and 0.85) Cathode Material for Lithium-Ion Batteries. *J. Power Sources* **2013**, *233*, 121–130. [[CrossRef](#)]
22. Sun, H.H.; Choi, W.; Lee, J.K.; Oh, I.H.; Jung, H.G. Control of Electrochemical Properties of Nickel-Rich Layered Cathode Materials for Lithium Ion Batteries by Variation of the Manganese to Cobalt Ratio. *J. Power Sources* **2015**, *275*, 877–883. [[CrossRef](#)]
23. Yoon, C.S.; Choi, M.H.; Lim, B.B.; Lee, E.J.; Sun, Y.K. Review—High-Capacity $\text{Li}[\text{Ni}_{1-x}\text{Co}_x/2\text{Mn}_{x/2}]\text{O}_2$ ($x = 0.1, 0.05, 0$) Cathodes for Next-Generation Li-Ion Battery. *J. Electrochem. Soc.* **2015**, *162*, A2483–A2489. [[CrossRef](#)]
24. Ishidzu, K.; Oka, Y.; Nakamura, T. Lattice Volume Change during Charge/Discharge Reaction and Cycle Performance of $\text{Li}[\text{Ni}_x\text{Co}_y\text{Mn}_z]\text{O}_2$. *Solid State Ionics* **2016**, *288*, 176–179. [[CrossRef](#)]
25. Friedrich, F.; Strehle, B.; Freiberg, A.T.S.; Kleiner, K.; Day, S.J.; Erk, C.; Piana, M.; Gasteiger, H.A. Editors' Choice—Capacity Fading Mechanisms of NCM-811 Cathodes in Lithium-Ion Batteries Studied by X-ray Diffraction and Other Diagnostics. *J. Electrochem. Soc.* **2019**, *166*, A3760–A3774. [[CrossRef](#)]
26. Yuan, K.; Li, N.; Ning, R.; Shen, C.; Hu, N.; Bai, M.; Zhang, K.; Tian, Z.; Shao, L.; Hu, Z.; et al. Stabilizing Surface Chemical and Structural Ni-rich Cathode via a Non-Destructive Surface Reinforcement Strategy. *Nano Energy* **2020**, *78*, 105239. [[CrossRef](#)]
27. Liu, T.; Yu, L.; Lu, J.; Zhou, T.; Huang, X.; Cai, Z.; Dai, A.; Gim, J.; Ren, Y.; Xiao, X.; et al. Rational Design of Mechanically Robust Ni-rich Cathode Materials via Concentration Gradient Strategy. *Nat. Commun.* **2021**, *12*, 6024. [[CrossRef](#)] [[PubMed](#)]
28. Park, N.Y.; Ryu, H.H.; Kuo, L.Y.; Kaghazchi, P.; Yoon, C.S.; Sun, Y.K. High-Energy Cathodes via Precision Microstructure Tailoring for Next-Generation Electric Vehicles. *ACS Energy Lett.* **2021**, *6*, 4195–4202. [[CrossRef](#)]
29. Lv, H.; Li, C.; Zhao, Z.; Wu, B.; Mu, D. A Review: Modification Strategies of Nickel-Rich Layer Structure Cathode ($\text{Ni} \geq 0.8$) Materials for Lithium Ion Power Batteries. *J. Energy Chem.* **2021**, *60*, 435–450. [[CrossRef](#)]
30. Lee, J.; Urban, A.; Li, X.; Su, D.; Hautier, G.; Ceder, G. Unlocking the Potential of Cation-Disordered Oxides for Rechargeable Lithium Batteries. *Science* **2014**, *343*, 519–522. [[CrossRef](#)]
31. Yabuuchi, N.; Nakayama, M.; Takeuchi, M.; Komaba, S.; Hashimoto, Y.; Mukai, T.; Shiiba, H.; Sato, K.; Kobayashi, Y.; Nakao, A.; et al. Origin of Stabilization and Destabilization in Solid-State Redox Reaction of Oxide Ions for Lithium-Ion Batteries. *Nat. Commun.* **2016**, *7*, 13814. [[CrossRef](#)] [[PubMed](#)]
32. Nakajima, M.; Yabuuchi, N. Lithium-Excess Cation-Disordered Rocksalt-Type Oxide with Nanoscale Phase Segregation: $\text{Li}_{1.25}\text{Nb}_{0.25}\text{V}_{0.5}\text{O}_2$. *Chem. Mater.* **2017**, *29*, 6927–6935. [[CrossRef](#)]
33. Zhao, X.; Tian, Y.; Lun, Z.; Cai, Z.; Chen, T.; Ouyang, B.; Ceder, G. Design Principles for Zero-Strain Li-ion Cathodes. *Joule* **2022**, *6*, 1654–1671. [[CrossRef](#)]
34. Cho, J.; Kim, Y.J.; Kim, T.J.; Park, B. Zero-Strain Intercalation Cathode for Rechargeable Li-Ion Cell. *Angew. Chem.* **2001**, *113*, 3471–3473. [[CrossRef](#)]
35. Kim, J.H.; Kim, H.; Choi, W.; Park, M.S. Bifunctional Surface Coating of LiNbO_3 on High-Ni Layered Cathode Materials for Lithium-Ion Batteries. *ACS Appl. Mater. Interfaces* **2020**, *12*, 35098–35104. [[CrossRef](#)]
36. Nguyen, A.; Zuo, P.; Jiang, H.; Wang, C.; Wang, D. Dual Protective Mechanism of AlPO_4 Coating on High-Nickel Cathode Material for High Energy Density and Long Cycle Life Lithium-Ion Batteries. *J. Electrochem. Soc.* **2022**, *169*, 050523. [[CrossRef](#)]
37. Mariyappan, S.; Marchandier, T.; Rabuel, F.; Iadecola, A.; Rousse, G.; Morozov, A.V.; Abakumov, A.M.; Tarascon, J.M. The Role of Divalent ($\text{Zn}^{2+}/\text{Mg}^{2+}/\text{Cu}^{2+}$) Substituents in Achieving Full Capacity of Sodium Layered Oxides for Na-Ion Battery Applications. *Chem. Mater.* **2020**, *32*, 1657–1666. [[CrossRef](#)]
38. Zhang, X.; Qiu, F.; Jiang, K.; He, P.; Han, M.; Guo, S.; Zhou, H. Improving the Structural and Cyclic Stabilities of P2-type $\text{Na}_{0.67}\text{MnO}_2$ Cathode Material via Cu and Ti Co-Substitution for Sodium Ion Batteries. *Chem. Commun.* **2020**, *56*, 6293–6296. [[CrossRef](#)]
39. Xin, F.; Zhou, H.; Zong, Y.; Zuba, M.; Chen, Y.; Chernova, N.A.; Bai, J.; Pei, B.; Goel, A.; Rana, J.; et al. What Is the Role of Nb in Nickel-Rich Layered Oxide Cathodes for Lithium-Ion Batteries? *ACS Energy Lett.* **2021**, *6*, 1377–1382. [[CrossRef](#)]
40. Kong, W.; Zhang, J.; Wong, D.; Yang, W.; Yang, J.; Schulz, C.; Liu, X. Tailoring Co3d and O2p Band Centers to Inhibit Oxygen Escape for Stable 4.6 V LiCoO_2 Cathodes. *Angew. Chem. Int. Ed.* **2021**, *60*, 27102–27112. [[CrossRef](#)]
41. Ou, X.; Liu, T.; Zhong, W.; Fan, X.; Guo, X.; Huang, X.; Cao, L.; Hu, J.; Zhang, B.; Chu, Y.S.; et al. Enabling High Energy Lithium Metal Batteries via Single-Crystal Ni-rich Cathode Material Co-Doping Strategy. *Nat. Commun.* **2022**, *13*, 2319. [[CrossRef](#)]
42. Kresse, G.; Furthmüller, J. Efficient Iterative Schemes for *Ab Initio* Total-Energy Calculations Using a Plane-Wave Basis Set. *Phys. Rev. B* **1996**, *54*, 11169–11186. [[CrossRef](#)]
43. Kresse, G.; Furthmüller, J. Efficiency of *Ab-Initio* Total Energy Calculations for Metals and Semiconductors Using a Plane-Wave Basis Set. *Comput. Mater. Sci.* **1996**, *6*, 15–50. [[CrossRef](#)]
44. Kresse, G.; Joubert, D. From Ultrasoft Pseudopotentials to the Projector Augmented-Wave Method. *Phys. Rev. B* **1999**, *59*, 1758–1775. [[CrossRef](#)]
45. Blöchl, P.E. Projector Augmented-Wave Method. *Phys. Rev. B* **1994**, *50*, 17953–17979. [[CrossRef](#)]
46. Monkhorst, H.J.; Pack, J.D. Special Points for Brillouin-zone Integrations. *Phys. Rev. B* **1976**, *13*, 5188–5192. [[CrossRef](#)]
47. Sun, J.; Ruzsinszky, A.; Perdew, J.P. Strongly Constrained and Appropriately Normed Semilocal Density Functional. *Phys. Rev. Lett.* **2015**, *115*, 036402. [[CrossRef](#)]
48. Sun, J.; Remsing, R.C.; Zhang, Y.; Sun, Z.; Ruzsinszky, A.; Peng, H.; Yang, Z.; Paul, A.; Waghmare, U.; Wu, X.; et al. Accurate First-Principles Structures and Energies of Diversely Bonded Systems from an Efficient Density Functional. *Nat. Chem.* **2016**, *8*, 831–836. [[CrossRef](#)] [[PubMed](#)]

49. Perdew, J.P.; Sun, J.; Martin, R.M.; Delley, B. Semilocal Density Functionals and Constraint Satisfaction. *Int. J. Quantum. Chem.* **2016**, *116*, 847–851. [[CrossRef](#)]
50. Zhang, Y.; Kitchaev, D.A.; Yang, J.; Chen, T.; Dacek, S.T.; Sarmiento-Pérez, R.A.; Marques, M.A.L.; Peng, H.; Ceder, G.; Perdew, J.P.; et al. Efficient First-Principles Prediction of Solid Stability: Towards Chemical Accuracy. *NPJ Comput. Mater.* **2018**, *4*, 9. [[CrossRef](#)]
51. Vydrov, O.A.; Van Voorhis, T. Nonlocal van Der Waals Density Functional: The Simpler the Better. *J. Chem. Phys.* **2010**, *133*, 244103. [[CrossRef](#)]
52. Dudarev, S.L.; Botton, G.A.; Savrasov, S.Y.; Humphreys, C.J.; Sutton, A.P. Electron-Energy-Loss Spectra and the Structural Stability of Nickel Oxide: An LSDA+U Study. *Phys. Rev. B* **1998**, *57*, 1505–1509. [[CrossRef](#)]
53. Perdew, J.P.; Burke, K.; Ernzerhof, M. Generalized Gradient Approximation Made Simple. *Phys. Rev. Lett.* **1996**, *77*, 3865–3868. [[CrossRef](#)]
54. Grimme, S.; Antony, J.; Ehrlich, S.; Krieg, H. A Consistent and Accurate *Ab Initio* Parametrization of Density Functional Dispersion Correction (DFT-D) for the 94 Elements H–Pu. *J. Chem. Phys.* **2010**, *132*, 154104. [[CrossRef](#)]
55. Fonseca Guerra, C.; Handgraaf, J.W.; Baerends, E.J.; Bickelhaupt, F.M. Voronoi Deformation Density (VDD) Charges: Assessment of the Mulliken, Bader, Hirshfeld, Weinhold, and VDD Methods for Charge Analysis. *J. Comput. Chem.* **2004**, *25*, 189–210. [[CrossRef](#)]
56. Tabuchi, M.; Tsutsui, S.; Masquelier, C.; Kanno, R.; Ado, K.; Matsubara, I.; Nasu, S.; Kageyama, H. Effect of Cation Arrangement on the Magnetic Properties of Lithium Ferrites (LiFeO_2) Prepared by Hydrothermal Reaction and Post-annealing Method. *J. Solid State Chem.* **1998**, *140*, 159–167. [[CrossRef](#)]
57. Amatucci, G.G.; Tarascon, J.M.; Klein, L.C. CoO_2 , the End Member of the Li_xCoO_2 Solid Solution. *J. Electrochem. Soc.* **1996**, *143*, 1114. [[CrossRef](#)]
58. Bo, S.H.; Li, X.; Toumar, A.J.; Ceder, G. Layered-to-Rock-Salt Transformation in Desodiated Na_xCrO_2 ($x \approx 0.4$). *Chem. Mater.* **2016**, *28*, 1419–1429. [[CrossRef](#)]
59. Bruce, P.G.; Armstrong, A.R.; Gitzendanner, R.L. New Intercalation Compounds for Lithium Batteries: Layered LiMnO_2 . *J. Mater. Chem.* **1999**, *9*, 193–198. [[CrossRef](#)]
60. Wang, X.; Li, Y. Synthesis and Formation Mechanism of Manganese Dioxide Nanowires/Nanorods. *Chem. Eur. J.* **2003**, *9*, 300–306. [[CrossRef](#)] [[PubMed](#)]
61. Sabitov, I.K. Algebraic Methods for Solution of Polyhedra. *Russ. Math. Surv.* **2011**, *66*, 445–505. [[CrossRef](#)]
62. Pearce, P.E.; Perez, A.J.; Rousse, G.; Saubanère, M.; Batuk, D.; Foix, D.; McCalla, E.; Abakumov, A.M.; Van Tendeloo, G.; Doublet, M.L.; et al. Evidence for Anionic Redox Activity in a Tridimensional-Ordered Li-rich Positive Electrode $\beta\text{-Li}_2\text{IrO}_3$. *Nat. Mater.* **2017**, *16*, 580–586. [[CrossRef](#)]

Disclaimer/Publisher’s Note: The statements, opinions and data contained in all publications are solely those of the individual author(s) and contributor(s) and not of MDPI and/or the editor(s). MDPI and/or the editor(s) disclaim responsibility for any injury to people or property resulting from any ideas, methods, instructions or products referred to in the content.